

SUPPORTING INFORMATION

Variable temperature and high-pressure crystal chemistry of perovskite formamidinium lead iodide: a single crystal X-ray diffraction and computational study

Shijing Sun,^a Zeyu Deng,^a Yue Wu,^a Fengxia Wei,^{a,b} Furkan Halis Isikgor,^c Federico Brivio,^a Michael W. Gaultois,^d Jianyong Ouyang,^c Paul D. Bristowe,^a Anthony K. Cheetham*^a, Gregor Kieslich*^{a,e}

^a Department of Materials Science and Metallurgy, University of Cambridge, 27 Charles Babbage Road, Cambridge CB3 0FS, U.K.

^b Institute of Materials Research and Engineering, Agency for Science, Technology and Research, 2 Fusionopolis Way, Singapore.

^c Department of Materials Science and Engineering, National University of Singapore, Singapore.

^d Department of Chemistry, University of Cambridge, Lensfield Rd, Cambridge CB2 1EW, UK

^e Department of Chemistry, Technical University of Munich, Lichtenbergstrasse 4, 85748 Garching, Germany.

Synthesis of [(NH₂)₂CH]PbI₃ Single Crystals

1 M of [(NH₂)₂CH]PbI₃ solution was prepared in γ -butyrolactone. The solution was filtered into a vial by using a polytetrafluoroethylene filter with pore size of 0.2 μm . The filtrate was then immersed in a silicon oil bath, which was pre-heated to 90 °C. The temperature of the system was slowly increased to 100 °C. Several black [(NH₂)₂CH]PbI₃ single crystals were collected at this temperature. The remnant solution was dissolved, filtered, and then immersed again in the silicon oil bath at 90 °C. The collected single crystals were used as seeds by gently placing them into the perovskite solution. Then, the temperature of the system was gradually increased 1 °C every 30 minutes to further increase the crystal size.

Single crystal X-ray Diffraction

Variable temperature single crystal X-ray diffraction measurements were performed on an Oxford Diffraction Gemini E Ultra diffractometer with an Eos CCD detector using Mo K α radiation ($\lambda = 0.7107 \text{ \AA}$). The crystals were cut to 0.2 mm in size and mounted on a cryoloop using perfluorinated oil. Data were collected using ω scans at temperatures of 100 K – 450 K in a nitrogen stream (started from 300K, heated up to 450 K, cooled to 100 K and heated back to 300 K). Data collection and reduction were performed with CrysAlisPro (Version 1.171.34i, Agilent Technologies). Absorption corrections were applied using analytical methods with face indexing. The structures were solved with ShelXT and refined with ShelXL-97^{1,2}. Using the OLEX2 platform³, all non-hydrogen atoms were refined anisotropically and the electron density of hydrogen atoms were not able to be determined in the presence of heavy atoms such as Pb and I in X-ray diffraction. The disorder in carbon atoms was modelled with partial occupancies. Although twinning occurred as the phase transition from cubic to tetragonal takes place, the majority of the diffraction spots overlap (>70%). Hence final structural solutions were refined with one component

of the twins, allowing analytical absorption corrections, except at 100 K where the twinning becomes severe at low temperatures and the structure was not able to be deduced without a twin model. Further analysis on the data set of $T = 120$ K and $T = 100$ K show that the structure is not incommensurately modulated, since the modulation vectors are $(0.33, 0.33, 0)$, $(-0.33, 0.33, 0)$ and $(0, 0, 0.167)$ respectively, which are special positions.

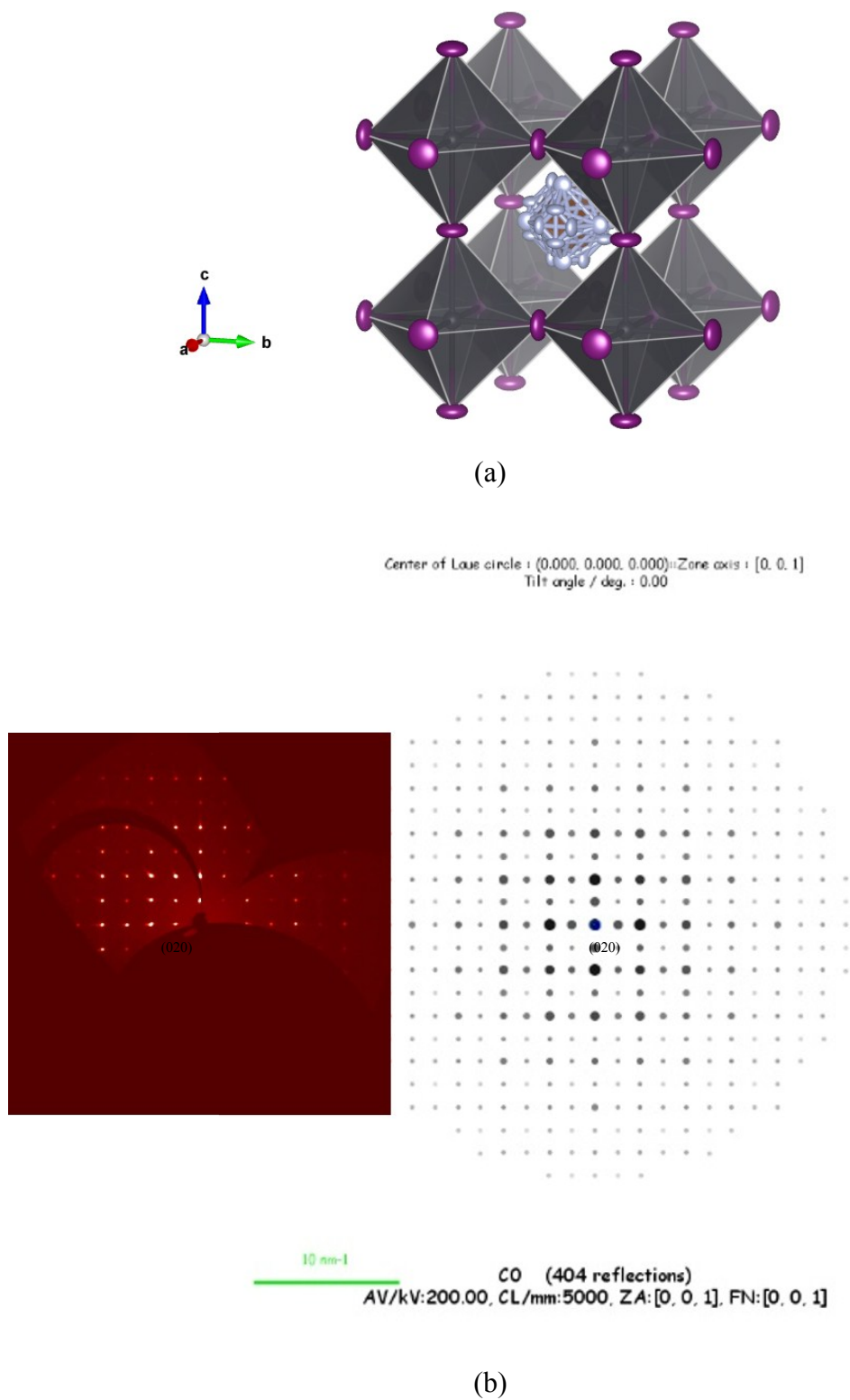


Fig. S1 (a) Crystal structure of $[(\text{NH}_2)_2\text{CH}]\text{PbI}_3$ at 300 K, iodide ions form ellipsoids (shown with 50% probability) that are perpendicular to the Pb-Pb vector in the cubic plane. Grey spheres represent lead,

purple represent iodide, carbon (brown) and nitrogen (blue) are modelled with disorder inside the perovskite cage. (b) X-ray diffraction patterns along [001] of $[(\text{NH}_2)_2\text{CH}]\text{PbI}_3$ at 300 K. The collected experimental pattern (left) is consistent with the simulated pattern using JEMS image simulation software (right) after structural solutions in the space group of $Pm\bar{3}m$.

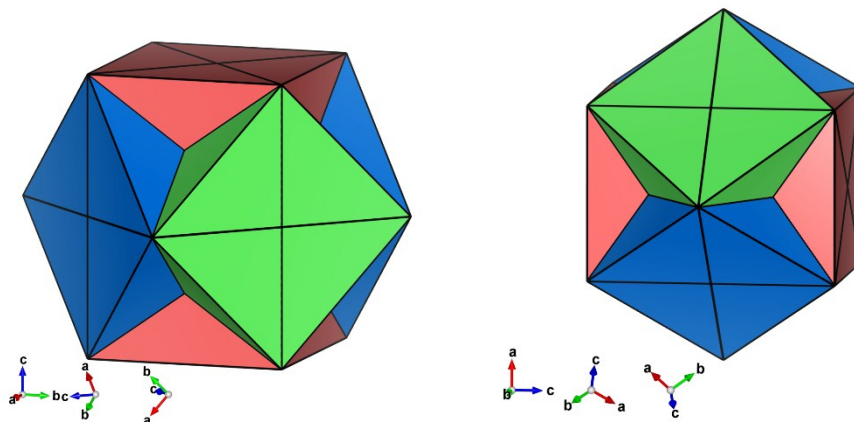
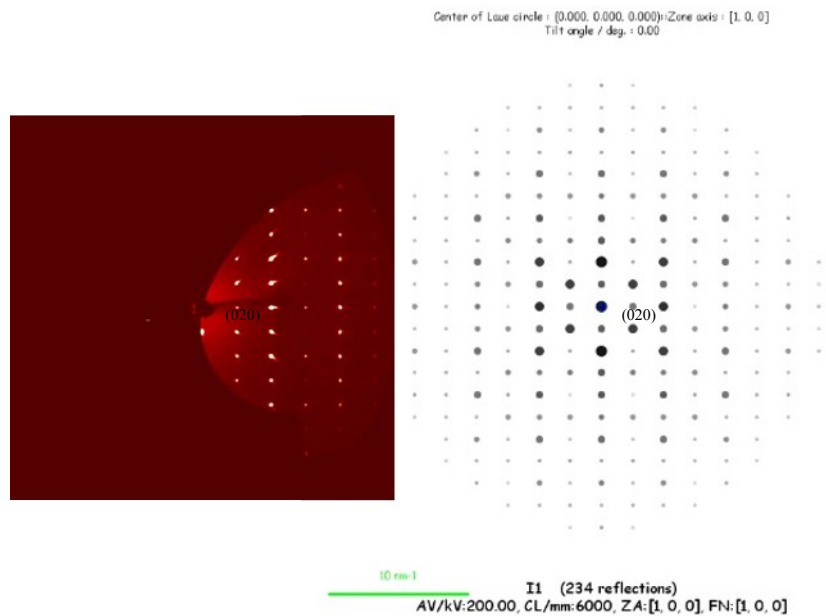


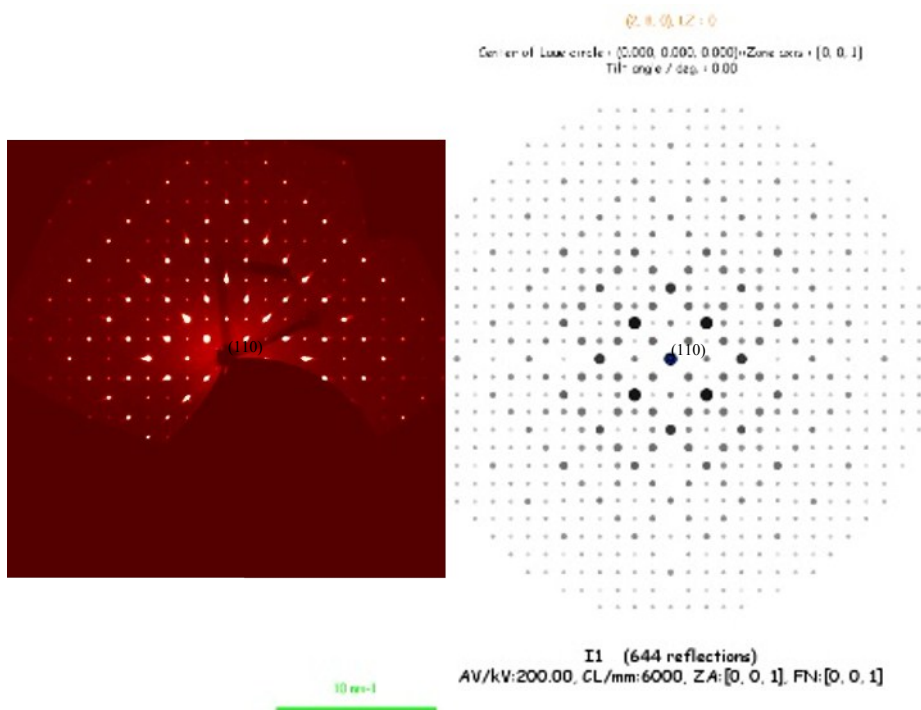
Fig. S2 Orientation relationship of three twins observed as the phase transition from cubic to tetragonal takes place. The surfaces of the twin components are represented in red, blue and green respectively.

One dataset collected at 250 K shows the three twins occupy 0.404, 0.333 and 0.264 of all the diffraction reflections respectively and the twin matrix is the following:

1	1.0000	0.0000	0.0000	0.0000	1.0000	0.0000	0.0000	0.0000	1.0000
2	-0.4998	0.5000	0.9993	0.5002	-0.5007	0.9995	0.5010	0.5005	0.0003
3	0.4988	-0.5004	-0.9988	0.4991	-0.5002	0.9968	-0.5009	-0.5010	0.0000



(a)



(b)

Fig. S3 Experimental and simulated X-ray diffraction patterns of $[(\text{NH}_2)_2\text{CH}]\text{PbI}_3$ at 250 K along $[100]$ shown in (a) and along $[001]$ shown in (b). The collected experimental patterns (left) are consistent with the simulated patterns using JEMS (right) respectively after structural solutions in $P4/mbm$. Most reflections from different components of the twins overlap, however, the intensities of the reflections are influenced by the intensities of different twinning components.

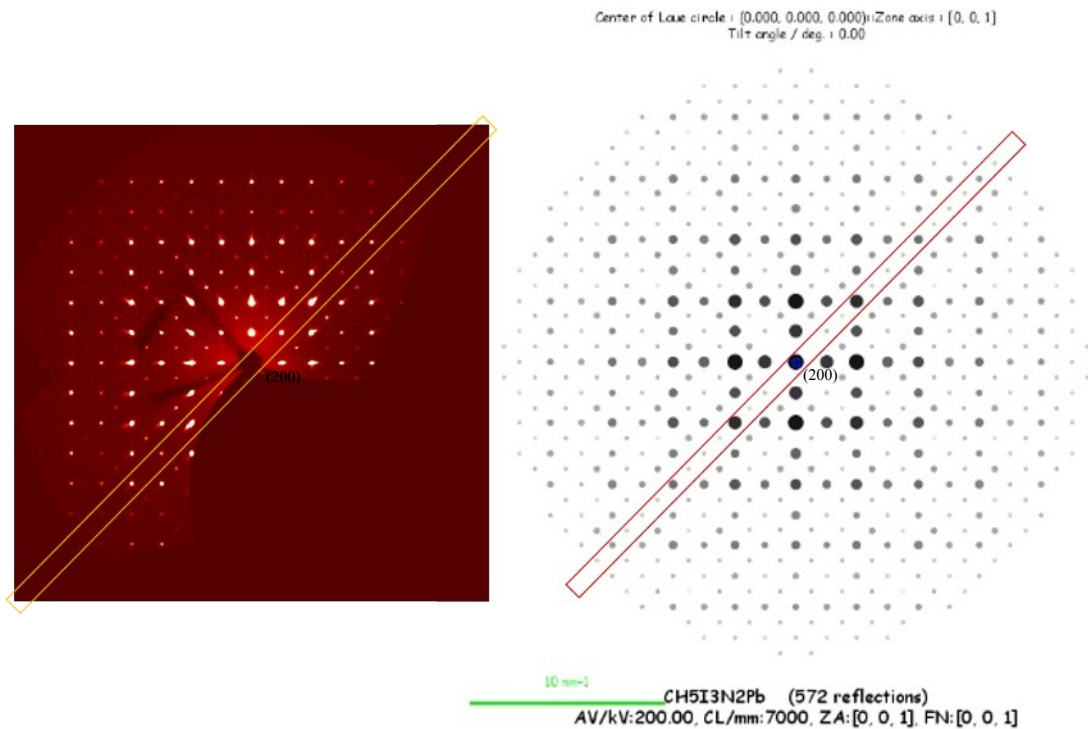


Fig. S4 The structure of $[(\text{NH}_2)_2\text{CH}]\text{PbI}_3$ at 250 K was solved in $Im\bar{3}$ ($a = b = c = 12.6895(8)$ Å), $R_{\text{wp}} = 5.62\%$, and X-ray patterns are shown along $[001]$. The collected experimental pattern (left) reveals systematic absences along $(hh0)$ where h is odd (highlighted in rectangle). However, reflections are expected at these positions in the simulated patterns using JEMS (right).

Table S1 Details of change in lattice parameters with temperature

	Temperature (K)	$a(\text{\AA})$	$c(\text{\AA})$	Unit Cell Volume (\AA^3)
1	300	6.3566(2)		256.84(1)
2	450	6.4009(5)		262.25(4)
3	400	6.3936(4)		261.36(3)
4	350	6.3806(3)		259.77(2)
5	300	6.3667(2)		258.07((2)
6	250	8.9710(7)	6.3427(8)	510.45(9)
7	200	8.9491(6)	6.3283(6)	506.80(7)
8	150	8.9267(6)	6.3126(6)	503.03(7)
9	120	8.8869(3)	6.2854(5)	496.40(5)
10	100	8.8750(20)	6.2820(30)	494.90(3)

Thermal Expansion:

Cubic 350 K – 450 K ($10^{-5}/\text{K}$): $\alpha_a = 3.2$, $\alpha_v = 9.6$

Tetragonal 150 K – 250 K ($10^{-5}/\text{K}$): $\alpha_a = 4.9$, $\alpha_c = 4.8$, $\alpha_v = 14.8$

Table S2 Details of the structure solution using variable temperature X-ray diffraction.

Empirical formula	CN ₂ PbI ₃ ¹			
Formula weight	632.96			
Crystal size/mm ³	0.24 × 0.14 × 0.06			
Radiation	MoK α (λ = 0.71073)			
Crystal system	Cubic	Tetragonal		
Space group	<i>Pm</i> $\bar{3}$ <i>m</i>	<i>P4</i> / <i>mbm</i>		
Z	1	2		
F(000)	266	522		
Temperature (K)	299.95(10)	150.00 (14)	200.00 (14)	249.95 (10)
a/Å	6.3667(2)	8.9267(6)	8.9491(6)	8.9710(7)
b/Å	6.3667(2)	8.9267(6)	8.9491(6)	8.9710(7)
c/Å	6.3667(2)	6.3126(6)	6.3283(6)	6.3427(8)
α /°	90	90	90	90
β /°	90	90	90	90
γ /°	90	90	90	90
Volume/Å ³	258.07(2)	503.03(8)	506.81(8)	510.45(10)
Density (calculated) /gcm ⁻³	4.073	4.146	4.115	4.092
μ /mm ⁻¹	25.243	25.9	25.706	25.523
2 θ range for data collection/°	6.4 to 55.678	6.454 to 56.202	6.438 to 56.048	6.422 to 55.902
Index ranges	-3 ≤ h ≤ 8, -8 ≤ k ≤ 1, -3 ≤ l ≤ 8	-9 ≤ h ≤ 10, -3 ≤ k ≤ 11, -8 ≤ l ≤ 1	-11 ≤ h ≤ 3, -10 ≤ k ≤ 9, -1 ≤ l ≤ 8	-10 ≤ h ≤ 9, -11 ≤ k ≤ 3, -8 ≤ l ≤ 1
Reflections collected	584	1051	1064	1089
Independent reflections	90 [R _{int} = 0.0771, R _{sigma} = 0.0439]	337 [R _{int} = 0.0445, R _{sigma} = 0.0423]	343 [R _{int} = 0.0445, R _{sigma} = 0.0472]	346 [R _{int} = 0.0420, R _{sigma} = 0.0403]
Data/restraints/parameters	90/0/9	337/14/14	343/3/14	346/3/18
Goodness-of-fit on F ²	1.025	1.128	1.293	1.055
Final R indexes [I ≥ 2 σ (I)]	R ₁ = 0.0442, wR ₂ = 0.1065	R ₁ = 0.0648, wR ₂ = 0.1579	R ₁ = 0.0629, wR ₂ = 0.1948	R ₁ = 0.0445, wR ₂ = 0.1159
Final R indexes [all data]	R ₁ = 0.0532, wR ₂ = 0.1386	R ₁ = 0.0781, wR ₂ = 0.1677	R ₁ = 0.0776, wR ₂ = 0.2072	R ₁ = 0.0655, wR ₂ = 0.1323
Largest diff. peak/hole / e Å ⁻³	0.82/-2.32	4.11/-3.02	3.00/-2.31	2.31/-1.46

¹H positions were not considered in the structural solution due to the difficulty of detecting light H in the presence of heavy Pb and I in X-ray diffraction

Table S3 Fractional Atomic Coordinates and Equivalent Isotropic Displacement Parameters (\AA^2) for low temperature phases. U_{eq} is defined as 1/3 of the trace of the orthogonalized UIJ tensor.

		Atom	x	y	z	Occupancy	U	Symmetry
300K	1	Pb	0.500	0.500	0.500	1	0.046	m-3m
	2	I1	0.000	0.500	0.500	1	0.046	4/mmm
250K	1	Pb	0.000	0.000	0.500	1	0.034	4/m
	2	I1	0.000	0.000	0.000	1	0.094	4/m
	3	I2	0.236	0.736	0.500	1	0.087	m2m
	4	N	0.600	0.100	0.000	1	0.370	m2m
	5	C	0.000	0.500	0.118	0.5	0.167	m2m
		Atom	x	y	z	Occupancy	U	Symmetry
200K	1	Pb	0.000	0.000	0.500	1	0.033	4/m
	2	I1	0.000	0.000	0.000	1	0.089	4/m
	3	I2	0.230	0.730	0.500	1	0.098	m2m
	4	N	0.602	0.102	0.000	1	0.210	m2m
	5	C	0.000	0.500	0.108	0.5	0.090	2mm
		Atom	x	y	z	Occupancy	U	Symmetry
150K	1	Pb	0.000	0.000	0.500	1	0.027	4/m
	2	I1	0.000	0.000	0.000	1	0.088	4/m
	3	I2	0.227	0.727	0.500	1	0.095	m2m
	4	N	0.601	0.101	0.000	1	0.943	m2m
	5	C	0.000	0.500	0.109	0.5	0.220	m2m

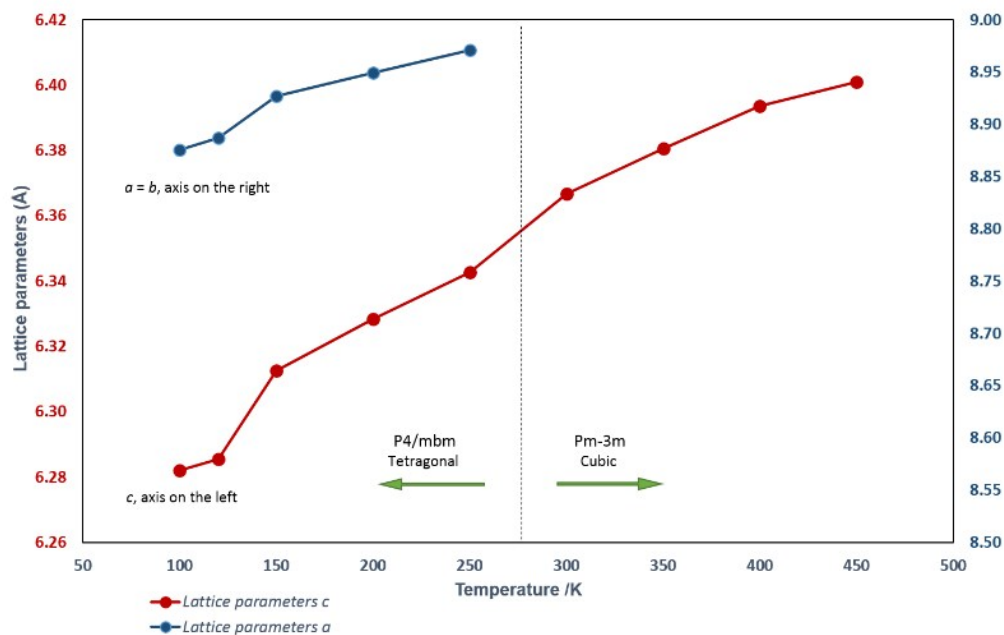


Fig. S5 Change in lattice parameters as a function of temperature. A cubic to tetragonal phase transition was observed on cooling from 300 K to 250 K and a second phase transition was observed below 150 K.

Ab initio molecular dynamics simulations

The ab initio molecular dynamics (MD) simulations were performed using the VASP code⁴. Projected augmented wave (PAW)⁴ potentials were used for Pb ($5d^{10}6s^26p^2$) and I ($5s^25p^5$), and the PBE functional⁵ with van der Waals correction⁶ was used to model the exchange-correlation. A 400 eV planewave kinetic energy cutoff and a Γ point only k-point mesh were used. Relativistic spin-orbit coupling (SOC) was not considered for the ab initio MD since it does not affect structural properties significantly⁷. The simulations were only performed on the 200 K $[(\text{NH}_2)_2\text{CH}]\text{PbI}_3$ structure with its unit cell doubled ($2 \times 2 \times 2$, 16 formula units). The experimental lattice parameters and positions of the inorganic elements (Pb and I) were all kept fixed during the simulations which were first performed for 10 ps to equilibrate the structure and then these data were discarded. Following this a further simulation of 50 ps was performed to collect data for analysis. The trajectories were sampled every 10 fs to determine the preferred orientations of the $[(\text{NH}_2)_2\text{CH}]^+$ ion.

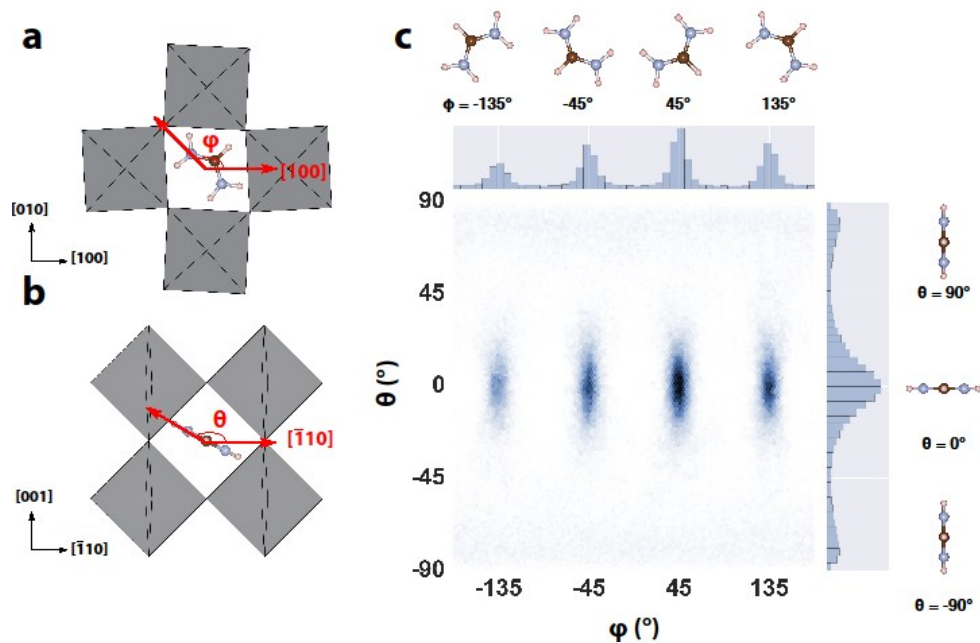


Fig. S6 Statistical analysis of the orientation of the $[(\text{NH}_2)_2\text{CH}]^+$ cation based on its N-N axis. Results determined from ab initio MD simulations. The angles ϕ and θ shown in (a) and (b) define the orientation of the N-N axis with respect to [100] and $[\bar{1}10]$ respectively. The results are equivalent to those shown in Figure 1 of the main text which use the C-H vector to define the orientation of the cation. The statistical distribution of ϕ and θ is shown in (c).

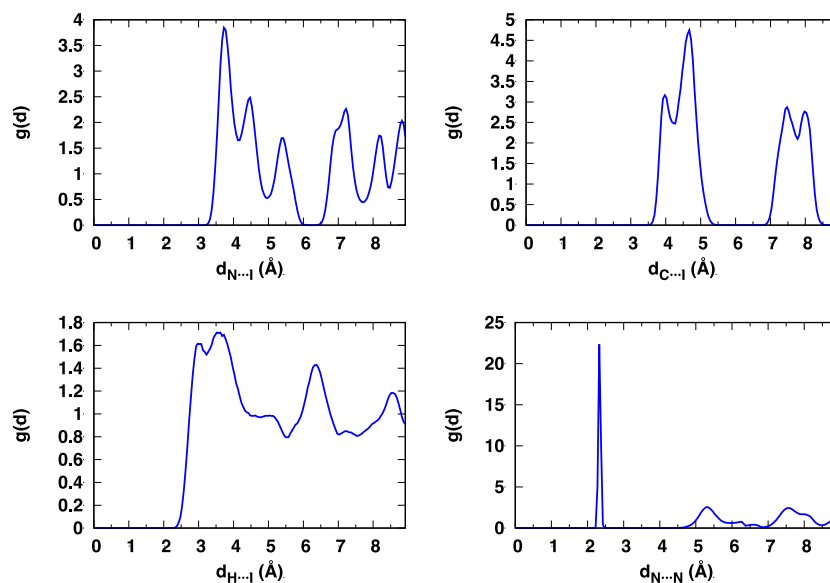


Fig. S7 Radial distribution functions (RDF) $g(d)$ of various interatomic distances determined from the ab initio MD simulations. The RDF calculations used a step size of 0.005 Å.

Table S3 First order (nearest neighbor) peak positions (Å) obtained from the RDF analysis in Fig. S7

N...I ¹	C...I ²	H...I	N...N
3.73	3.98	3.08	2.33

¹ Bond distances from X-ray diffraction: 3.70(1) Å at T = 250 K and 3.68 (1) Å at T = 200 K.

² Bond distances from X-ray diffraction: 3.85(1) Å at T = 250 K and 3.83 (2) Å at T = 200 K.

Ground state DFT calculations of the cation orientation

The DFT calculations were performed using the VASP code⁸ with the same PAW potentials as used for the ab initio MD simulations and a very similar exchange correlation functional (PBEsol). A plane-wave kinetic energy cutoff of 500 eV was employed together with a 4 x 4 x 2 k-point mesh. An extended supercell with dimensions $\sqrt{2}a \times \sqrt{2}a \times 2a$ was constructed with the $[(\text{NH}_2)_2\text{CH}]^+$ cations initially placed in different starting orientations within the perovskite cage. Geometry optimization of the internal atomic positions was then performed. This resulted in different final structures, with the $[(\text{NH}_2)_2\text{CH}]^+$ cations inducing different tilting of the octahedral due to the strong interplay between the cage and the organic cation. Selected VASP input and output files for the MD and ground state calculations are located at <https://doi.org/10.17863/CAM.10455>.

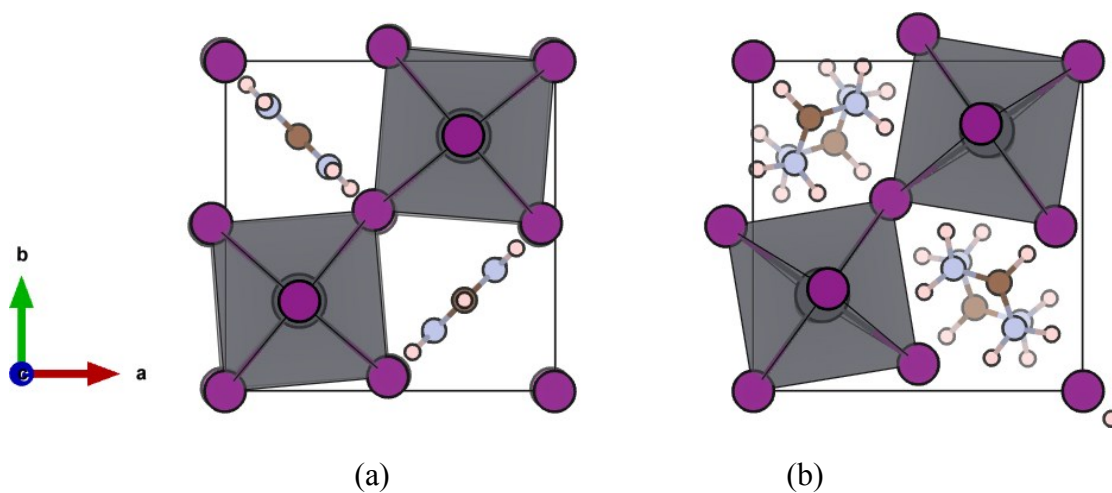


Fig. S8 Orientations of the $[(\text{NH}_2)_2\text{CH}]^+$ cations in relation to the perovskite cage and the octahedral tilting, with (a) tilting in the ab -plane and (b) tilting about the c direction.

Fig. S8 (a) shows the most stable structure found and exhibits a $[(\text{NH}_2)_2\text{CH}]^+$ orientation consistent with the experimental data (i.e. the same as Figure 1(a) of the main text with $\varphi = 45^\circ$ and $\theta = 0^\circ$). Here the C-H bond is parallel to the c -axis and there is no octahedral tilting about this direction. SI-Figure 8(b) shows a structure with slightly higher energy (70 meV/f.u.) where the C-H bond lies in the ab -plane. In this case the optimization also produced some octahedral tilting about the c -axis that is not observed experimentally. The small energy difference between the two structures could indicate the presence of lower symmetry phases at low temperatures, where the orientation of the organic cation is quenched.

Ground state DFT calculations of electronic structure

The DFT calculations were performed using the VASP code⁸ with the same PAW potentials and exchange correlation functional as used for the ab initio MD simulations. A plane-wave kinetic energy cutoff of 500 eV was employed. For the density of states (DOS) calculations a $10 \times 10 \times 12$ k-point mesh was used. Relativistic spin-orbit coupling (SOC) is important in this system and was considered for both the band structure and DOS calculations.⁹ Because the electronic structure of $[(\text{NH}_2)_2\text{CH}]\text{PbI}_3$ near the band gap depends mostly on the inorganic elements, i.e. Pb and I, the experimental lattice parameters and ionic positions of Pb and I at different temperatures were fixed throughout the calculations, and $[(\text{NH}_2)_2\text{CH}]^+$ was replaced by a positive background charge. The background charge avoids considering the orientational disorder of the cation.

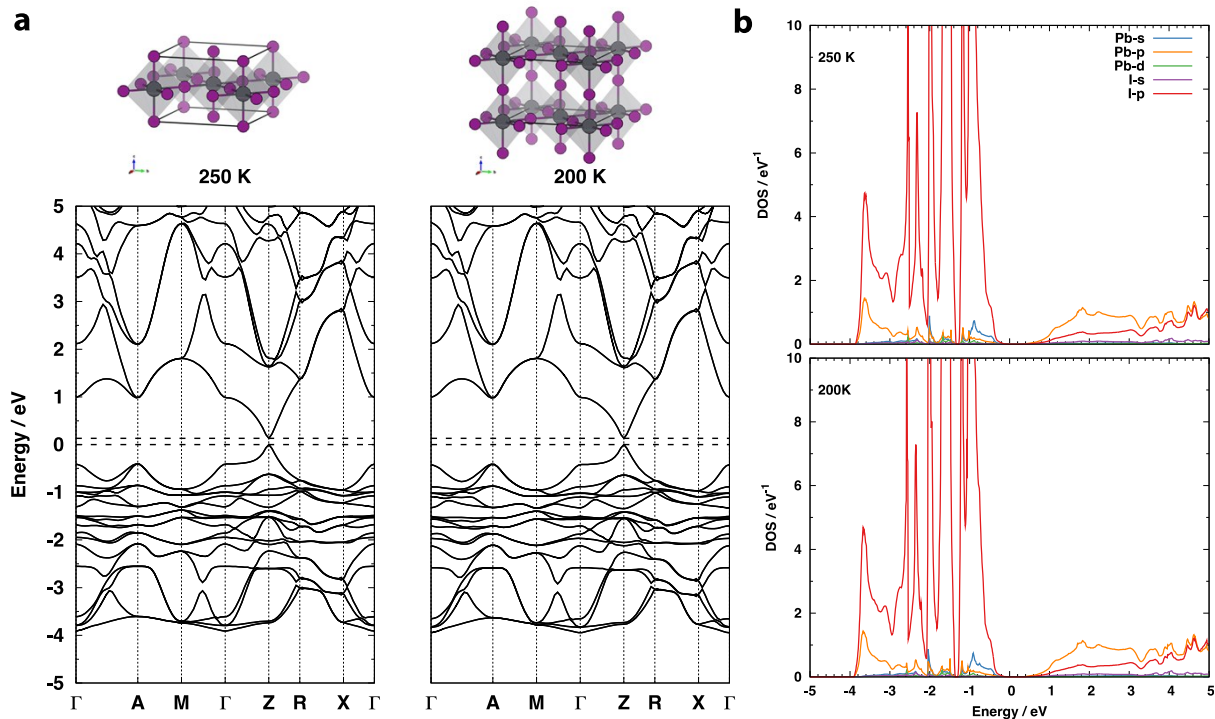


Fig. S9 Comparison of the calculated band structure and DOS of $[(\text{NH}_2)_2\text{CH}]\text{PbI}_3$ at 250 K and 200 K in which the $[(\text{NH}_2)_2\text{CH}]^+$ cation has been replaced by a positive background charge. The following high symmetry path for a primitive tetragonal lattice was used for the band structure calculations: $\Gamma(0,0,0)$, $A(0.5,0.5,0.5)$, $M(0.5,0.5,0)$, $\Gamma(0,0,0)$, $Z(0,0,0.5)$, $R(0,0.5,0.5)$, $X(0,0.5,0)$ and $\Gamma(0,0,0)$.

Fig. S9 shows the DFT calculated electronic band structure and DOS of $[(\text{NH}_2)_2\text{CH}]\text{PbI}_3$ using the experimentally determined $[\text{PbI}_3]^-$ framework at two different temperatures: 250 K and 200 K. It is acknowledged that DFT+SOC will underestimate the band gap significantly and improved band gap values could be achieved using the GW method.¹⁰ The DFT calculated band gaps are very similar and about 0.131 eV for both structures. From 250 K to 200 K, the a and c lattice constants reduced by ~ 0.023 Å and ~ 0.015 Å respectively and the concomitant small change in Pb-I bond lengths makes their band structures look almost the same. From the projected density of states, it can be seen that the valence band edge consists mostly by Pb 6s - I 5p antibonding states whereas the conduction band edge consists mostly of Pb 6p - I 5p antibonding states, which is similar to previous studies.^{11,12}

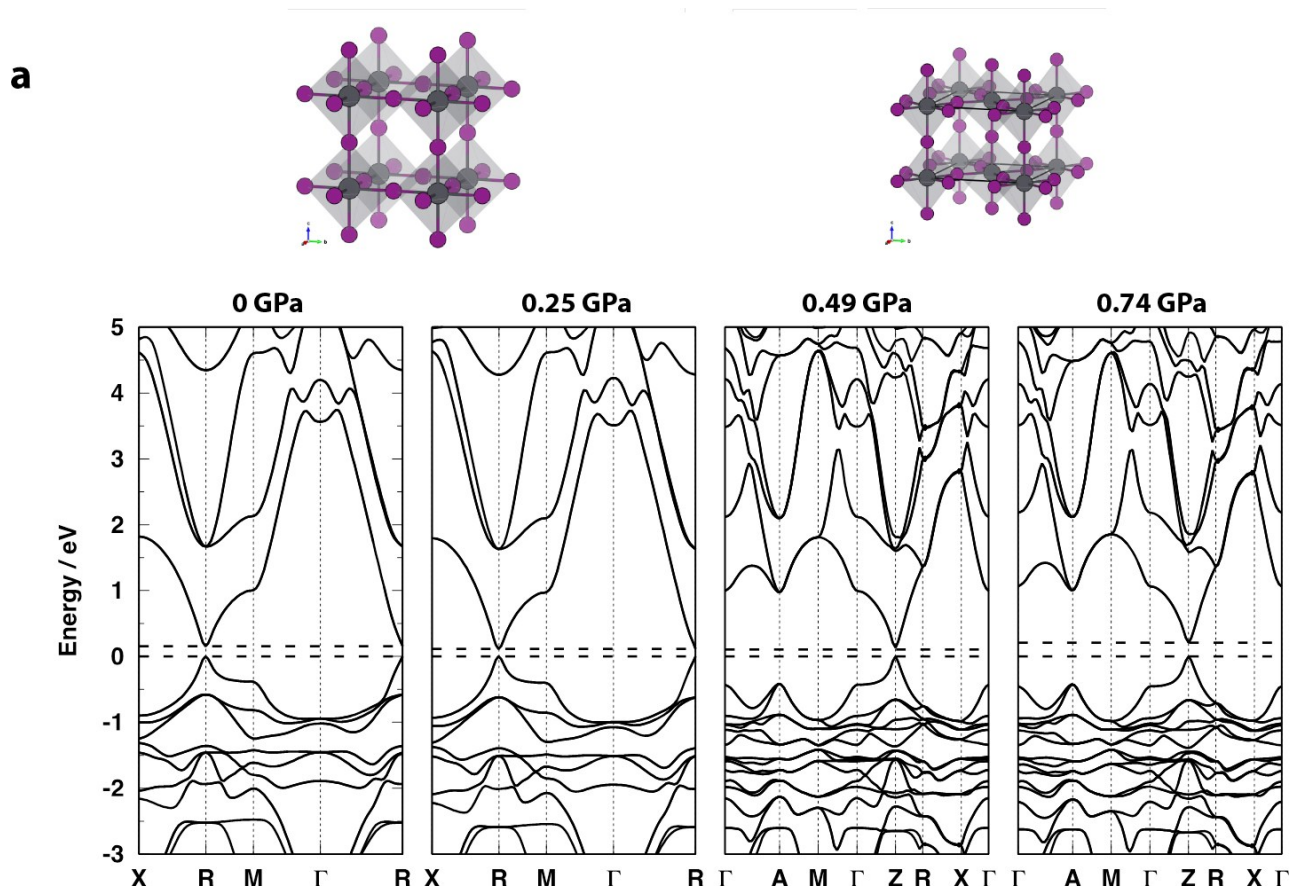


Fig. S10 Comparison of the calculated band structure and DOS of $[(\text{NH}_2)_2\text{CH}]\text{PbI}_3$ at four different hydrostatic pressures (ambient – 0.74 GPa) in which the $[(\text{NH}_2)_2\text{CH}]^+$ cation has been replaced by a positive background charge. The following high symmetry path was used for the primitive cubic structures $X(0.5,0,0)$, $R(0.5,0.5,0.5)$, $M(0.5,0.5,0)$ and $\Gamma(0,0,0)$ while for the primitive tetragonal structures it was $\Gamma(0,0,0)$, $A(0.5,0.5,0.5)$, $M(0.5,0.5,0)$, $\Gamma(0,0,0)$, $Z(0,0,0.5)$, $R(0,0.5,0.5)$, $X(0,0.5,0)$ and $\Gamma(0,0,0)$.

Fig. S10 shows the DFT calculated electronic band structure and DOS of $[(\text{NH}_2)_2\text{CH}]\text{PbI}_3$ using the experimentally determined $[\text{PbI}_3]^-$ framework at four different hydrostatic pressures. The calculated band gaps are 0.148 eV, 0.116 eV, 0.135 eV and 0.210 eV at 0 GPa, 0.25 GPa, 0.49 GPa and 0.74 GPa structure, respectively. Note that $[(\text{NH}_2)_2\text{CH}]\text{PbI}_3$ is tetragonal at 0.494 GPa and 0.741 GPa. In the absence of octahedral tilting, a reduction in Pb-I bond lengths under pressure will shift the Pb-I antibonding energy states that dominate the band edges and reduce the band gap. This will be particularly apparent for the occupied states near the valence band edge which will increase their energy.¹³ Increasing the pressure from ambient to 0.25 GPa reduces the lattice constant by $\sim 0.027 \text{ \AA}$, which leads to a drop in band gap of $\sim 0.03 \text{ eV}$. Further increase of pressure to 0.49 GPa continues to reduce the Pb-I bond lengths and although the octahedra begin to tilt and the structure becomes tetragonal, the band gap is still smaller than the value at the ambient condition. Band gap reduction due to shorter Pb-I bond lengths and band gap enlargement due to octahedral tilting are clearly competitive effects and can co-exist. This is evident when the pressure increases to 0.74 GPa because octahedral tilting becomes the dominant effect and the band gap increases to a value greater than at ambient pressure.

High Pressure X-ray Crystallography

High-pressure single crystal diffraction experiments were performed using a diamond anvil cell setup at the Diamond Light Source (I19, $\lambda = 0.4895 \text{ \AA}$), with Fluorinert FC-70 as an inert pressure transmitting medium. The fluorescence of ruby was used for pressure calibration.

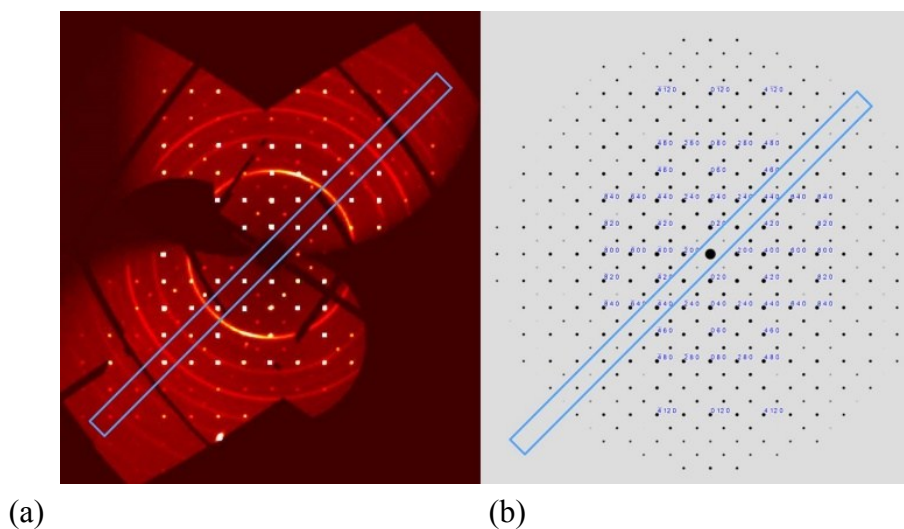


Fig. S11 In order to investigate systematic absences in the high-pressure SCXRD datasets, the zero diffraction plane of black $[(\text{NH}_2)_2\text{CH}]\text{PbI}_3$ are compared: (a) experimental and (b) simulated after structure solution in Im-3 . A R_{wp} value of 9.8 % and systematic absences not in agreement with Im-3 (highlighted with the blue boxes) indicate that Im-3 is likely to be a wrong assignment.

Table S4. Details of the structure solution for the high-pressure experiments. Note that, as explained in the main text, the phase transition that occurs between $p = 0.25$ GPa and 0.49 GPa is related to twinning of the crystal, which makes structure solution extremely challenging.


Crystal size/mm ³	every axis smaller than 100 μ m			
				
Radiation	Synchrotron radiation $\lambda = 0.4859$ Å			
pressure	ambient	0.25 GPa	0.49 GPa	0.74 GPa
Formula	N ₂ CPbI ₃	N ₂ CPbI ₃	PbI ₃	PbI ₃
Z	1	1	2	2
Crystal system	Cubic	Cubic	Tetragonal	Tetragonal
Space-group	<i>Pm</i> $\bar{3}$ <i>m</i>	<i>Pm</i> $\bar{3}$ <i>m</i>	<i>P4</i> / <i>mbm</i>	<i>P4</i> / <i>mbm</i>
a/Å	6.36803(16)	6.34132(13)	8.9148(6)	8.8430(6)
b/Å	6.36803(16)	6.34132(13)	8.9148(6)	8.8430(6)
c/Å	6.36803(16)	6.34132(13)	6.3138(7)	6.27090(6)
α /°	90	90	90	90
β /°	90	90	90	90
γ /°	90	90	90	90
Volume/Å ³	258.24(2)	255.00(16)	501.78(9)	491.01(8)
μ /mm ⁻¹	9.357	9.476	9.621	9.833
F(000)	261.0	261.0	482	482
2 Θ range for data collection/°	6.186 to 37	4.392 to 44.816	4.414 to 33.51	4.432 to 44.746
Index ranges	-8 \leq h \leq 8, -7 \leq k \leq 7, -9 \leq l \leq 8	-8 \leq h \leq 8, -9 \leq k \leq 9, -7 \leq l \leq 7	-10 \leq h \leq 10, -6 \leq k \leq 6, -7 \leq l \leq 7	-7 \leq h \leq 7, -13 \leq k \leq 13, -8 \leq l \leq 8
Reflections collected	1540	1532	1123	2338
Independent reflections	111 [R _{int} = 0.0379, R _{sigma} = 0.0123]	110 [R _{int} = 0.0474, R _{sigma} = 0.0156]	186 [R _{int} = 0.0392, R _{sigma} = 0.0138]	372 [R _{int} = 0.0568, R _{sigma} = 0.0285]
Data/restraints/parameters	111/0/9	110/0/9	186/0/9	372/0/9
Goodness-of-fit on F ²	1.145	1.218	1.137	1.317
Final R indexes [I \geq 2 σ (I)]	R ₁ = 0.0223, wR ₂ = 0.0586	R ₁ = 0.0257, wR ₂ = 0.0520	R ₁ = 0.0650, wR ₂ = 0.1928	R ₁ = 0.0679, wR ₂ = 0.2398
Largest diff. peak/hole / e Å ⁻³	0.63/-0.80	0.83/-0.87	2.31/-1.52	7.36/-6.04

Table S5. Fractional Atomic Coordinates ($\times 10^4$) and Equivalent Isotropic Displacement Parameters ($\text{\AA}^2 \times 10^3$) for formamidinium lead iodide at $p =$ ambient, 0.25 GPa, 0.49 GPa and 0.74 GPa. As explained in the text, for pressures higher than 0.25 GPa, atomic positions of the formamidinium cations within the electron rich $[\text{PbI}_3]^-$ cage were not assigned. U_{eq} is defined as 1/3 of the trace of the orthogonalised U_{II} tensor.

$p =$ ambient				
Atom	x	y	z	$U(\text{eq})$
Pb1	0	0	0	37.7(3)
I2	0	0	5000	91.5(5)
C1	5000	5000	5000	170(30)
N1	4260(80)	6680(110)	5000	80(20)
Pb-I-Pb angle: 180°				
$p =$ 0.25 GPa				
Atom	x	y	z	$U(\text{eq})$
Pb1	0	0	0	36.9(2)
I2	0	5000	0	104.0(6)
C1	5000	5000	5000	170(30)
N1	3260(120)	4270(110)	5000	110(30)
Pb-I-Pb angle: 180°				
$p =$ 0.49 GPa				
Atom	x	y	z	$U(\text{eq})$
Pb1	0	0	0	37.6(10)
I1	5000	5000	5000	102(3)
I2	7271(4)	7729(4)	10000	95.4(14)
Pb-I-Pb angle: $169.53(13)^\circ$				
$p =$ 0.74 GPa				
Atom	x	y	z	$U(\text{eq})$
Pb1	0	0	0	38.1(7)
I1	5000	5000	5000	79(2)
I2	2104(5)	2896(5)	10000	83.0(13)
Pb-I-Pb angle: $162.00(16)^\circ$				

References

- (1) Sheldrick, G. M. *Acta Cryst.* **2008**, *A64*, 112–122.

- (2) Sheldrick, G. M. . *Acta Cryst.* **2015**, *A71*, 3–8.
- (3) Dolomanov, O.V., Bourhis, L.J., Gildea, R.J, Howard, J.A.K. & Puschmann, H. *J. Appl. Cryst.* **2009**, *42*, 339–341.
- (4) Blöchl, P. E. *Phys. Rev. B* **1994**, *50* (24), 17953–17979.
- (5) Perdew, J. P.; Burke, K.; Ernzerhof, M. *Phys. Rev. Lett.* **1996**, *77* (18), 3865–3868.
- (6) Grimme, S. *J. Comput. Chem.* **2006**, *27* (15), 1787–1799.
- (7) Egger, D. A.; Kronik, L. *J. Phys. Chem. Lett.* **2014**, *5* (15), 2728–2733.
- (8) Kresse, G.; Furthmüller, J. *Phys. Rev. B* **1996**, *54* (16), 11169–11186.
- (9) Even, J.; Pedesseau, L.; Jancu, J.-M.; Katan, C. *J. Phys. Chem. Lett.* **2013**, *4* (17), 2999–3005.
- (10) Umari, P.; Mosconi, E.; De Angelis, F. *Sci. Rep.* **2014**, *4*.
- (11) Filippetti, A.; Mattoni, A. *Phys. Rev. B* **2014**, *89* (12), 125203.
- (12) Filip, M. R.; Eperon, G. E.; Snaith, H. J.; Giustino, F. *Nat. Commun.* **2014**, *5*, 5757.

